AIAA 80-0385R

Cross-Flow Propulsion Fan Experimental Development and Finite-Element Modeling

Gary J. Harloff* and Donald R. Wilson†
The University of Texas, Arlington, Texas

The cross-flow propulsion fan (CFF) is a novel two-dimensional, two-stage fan which can be integrated directly into a wing to provide both axial propulsive thrust and lift augmentation. The results of a recent experimental and theoretical development program improve the fan's performance in the transonic range and provide new insight into the flowfield. The overall performance of the CFF is presented in terms of conventional fan performance maps, together with detailed measurements of the interior flowfield. Analytical models based on finite-element modeling of the flow within the CFF produced good agreement with experimental data. The fan housing effects on the flowfield and overall performance are considered for the first time. The analytical model provides improved capability for designing CFF configurations that should lead to improved performance for future applications.

Nomenclature

$A, A^{(e)}$ = area, element area
A = geometry matrix
c = chord
C_p = specific heat at constant pressure
C_f = skin friction coefficient
D_H = hydraulic diameter
F_N = forcing function vector
f = rotor blade force
h = enthalpy, or dx for element n
i = incidence angle
L = fan span
$\dot{m}$ = mass flow
N = rotor speed
$N/\sqrt{\theta}$ = corrected rpm
Q = volume flow rate, or heat input
$\dot{q}_w$ = heat transfer due to convection
R = radius, or gas constant
R_p = total pressure ratio
R_e = Reynolds number
S = blade spacing
T = temperature, or torque
U = tip velocity
u, v = x, y velocity components
w = work input
w_z = angular velocity of rotor
W = weight flow
$W\sqrt{\theta}/\delta$ = corrected airflow
χ = longitudinal distance
α, β = absolute, relative flow angles
Γ = integration path
δ = P_t/P_{SL}, or deviation angle
η_H = hydraulic efficiency = $Q\Delta P$/input shaft power
θ = angular extent, or T_t/T_{SL}
ρ = density
τ_w = shear stress at wall
ϕ = flow coefficient, Q/U_0LH_E, or velocity potential
ϕ_i = interpolation polynomial at node i
ϕ_N = interpolation polynomial on a boundary
ψ = pressure coefficient $\Delta P/\frac{1}{2}\rho U^2$, or stream function
Ω = area, or angular frequency

Subscripts

1, 2 = inlet and outlet of first rotor
3, 4 = inlet and outlet of second rotor
D = diameter
HPC = high-pressure cavity
I = inlet
LPC = low-pressure cavity
R = rotor
r = radial
s = static
SL = sea level
t = tip or total
W = wall
z = longitudinal
θ = circumferential

Introduction

An example of a typical application of the cross-flow fan (CFF) to aircraft propulsion was given by Dornier[1] in 1962, and is shown in Fig. 1. Other examples for wing installations are shown in Fig. 2. In addition to providing thrust for cruise application, rotating the housing permits thrust vectoring for use in maneuvering or for vertical takeoff and landing applications. Aerodynamic circulation control is also possible. An advantage of the CFF for propulsion applications is its two-dimensional geometry. The length of the fan can be made arbitrarily long and is ideally suited for wing installation.

Review of Previous Experimental Studies and Performance

The CFF was invented in the early 1890s by P. Mortier, a French electrical engineer. The design was disclosed in patents in 1892[2] and 1893.[3]

Prior investigators have determined the effects of the external housing geometry, interior guidevanes, low-pressure cavity, exterior guide vanes, and the Reynolds number on fan performance. Few of these studies were comprehensive, and it is difficult to relate performance because of the strong interaction of the several parts of the housing.

Presented as Paper 80-0385 at the AIAA 18th Aerospace Sciences Meeting, Pasadena, Calif., Jan. 14-16, 1980; submitted Jan. 21, 1980; revision received May 30, 1980.

*Graduate Student (presently Project Engineer with Gulf Research). Member AIAA.

†Associate Professor of Aerospace Engineering. Associate Fellow AIAA.

A comprehensive review of the prior CFF literature is presented in Ref. 4. The overall CFF performance varies widely between different investigators, and ranges from $0 \leq \phi \leq 2$ and $0 \leq \psi \leq 5$.[5-11] The current test results vary from $0.6 \leq \phi \leq 1.0$ and $2 \leq \psi \leq 5$. The primary difference in performance between various designs is due to the different housing configurations. The experimental performance of the fans developed in the present program is characterized by higher pressure and lower flow coefficients relative to most of the data reported in the literature.

From the literature review[4] it was concluded that the housing geometry has a pronounced effect on the flowfield and the resulting performance. The low-pressure cavity (LPC) and the high-pressure exit housing are most influential, while internal guide vanes can also be used to influence the performance. The internal vortex strength is apparently dependent upon Reynolds number for values up to 20,000, based on Englehardt's data,[11] and independent of Reynolds number for values higher than 20,000. The output total pressure can be tuned to be independent of airflow through proper housing design. It is clear that the development of the CFF has been hampered by the sensitivity of its performance to the housing design. As will be discussed below, an adequate theoretical understanding of the flowfield has not yet been developed.

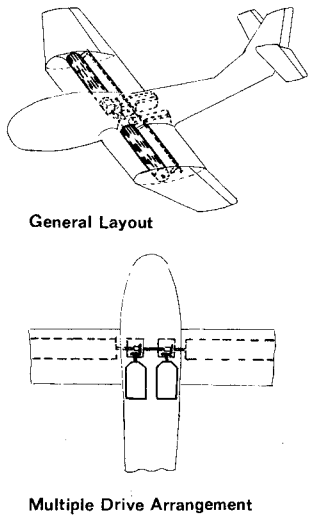

Fig. 1 Aircraft propulsion application (after Ref. 1).

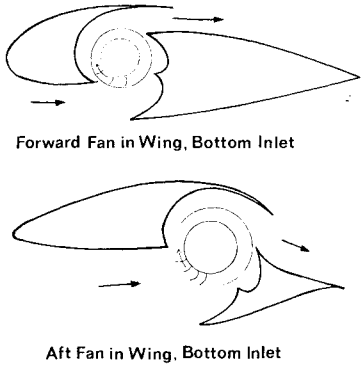

Fig. 2 Cross-flow fan in wing schematics.

Experimental Program

The purpose of the experimental program was to define and improve the performance of the CFF over a wide range of rpm and operating conditions. Several different fan blade designs were built and tested with a combination of housings. The fan variables consisted of outer blade angle β_o, inner blade angle β_i, diameter ratio D_i/D_o, number of blades or solidity, and the span. Table 1 gives the fan test variables for each fan. The fans were made of aluminum. The blades were circular arc sections because they pass flow in both directions. Ten fans with 30.48-cm diam and 3.81 cm spans and one fan with 30.48 cm diam and 30.48 cm span were tested.

The housing geometry development program consisted of an extensive literature survey, numerous water table tests, and air test rig evaluations of several hundred housing configurations. The housing variables tested include the inlet (I) and exit (E) arc, low-pressure cavity (LPC) arc, high-pressure cavity (HPC) arc, exit height (H_E), and exit shape. A typical fan housing design is shown in Fig. 3.

Performance Test Data

Fan performance was determined by varying the rpm and measuring airflow and total pressure and temperature rise. From these measurements the fan corrected airflow, total pressure ratio, and adiabatic compression efficiency were

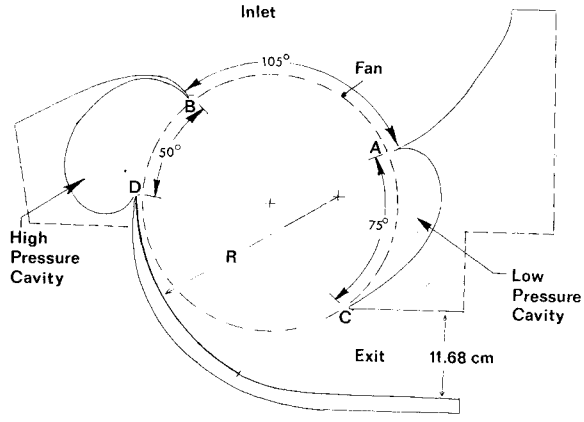

Fig. 3 Typical fan housing.

Table 1 Description of experimental fans tested

Fan No.	Span, cm	Outer blade angle, deg	Inner blade angle, deg	Number of blades	Diameter ratio	Solidity (chord/tip space)
1	3.81	45	0	16	0.70	0.830
2	3.81	53	−10	24	0.70	1.250
3	3.81	53	−10	36	0.80	1.241
4	3.81	53	−10	30	0.70	1.540
5	3.81	60	−10	30	0.70	1.540
6	3.81	60	−10	30	0.70	1.570
7	3.81	60	−10	36	0.74	1.630
8	3.81	65	−10	30	0.70	1.600
9	3.81	60	0	36	0.74	1.710
10[a]	30.48	60	−10	30	0.70	1.540

[a] Built per fan 5 specifications.

determined. Several exit areas were tested to generate conventional fan maps. The gain in fan performance achieved during an experimental development program consisting of nearly 800 test runs included gains in efficiency of 55-77%, corrected flow of 1.16-1.42 kg/s, and total pressure ratio of 1.2-1.4. The variables primarily responsible for the performance increase are, in order of decreasing importance: exit height, low-pressure cavity shape, inlet arc, exit housing, and fan blade design.

Fan Maps

Typical maps for fans 4 and 6 are shown in Figs. 4 and 5. Airflow choking is apparent with a 16.76 cm exit at 8000 rpm for fan 4 (Fig. 4). With an improved exit shape used for fan 6, constant total pressure ratio was obtained at various rpms, as shown in Fig. 5. Efficiency correlates with corrected airflow as shown at the top of Fig. 5.

Nondimensional Performance

Figure 6 presents the variation of hydraulic efficiency η_H and flow coefficient ϕ vs total pressure coefficient ψ_t for fans 6 and 9. As observed, increasing rpm decreases ϕ and ψ due to compressibility effects. Flow coefficients up to 2.0, total pressure coefficients up to 4.5, and efficiencies up to 0.8 are obtained and the correlation is independent of exit height for fan 9.

30.48 cm Span Fan Test Results

The 30.48 cm span fan (fan 10) was built and tested to determine scaling effects of the two-dimensional fan. It was built according to fan 5 specifications. Two disks were spaced 10.16 cm apart to provide structural support, as shown schematically in Fig. 7. The housing tested was the same shape as previously tested for fan 5, with a 10.16 cm exit.

Performance data for the 30.48 and 3.81 cm span fan 5 are compared in Fig. 8. The fan 5 data do not overlap exactly at 7000 and 8000 rpm because of the effect of removing the exit rakes from the exit duct. The 30.48 cm fan data provided higher performance in terms of total pressure rise and airflow. The efficiency is quantitatively similar.

Flowfield Survey

A schematic representation of the CFF flow is shown in Fig. 9. The airflow in the fan passes from inlet through the inlet rotors, interior, exit rotors, and exit. Two recirculation flows are bounded by the two cavities and the two separating

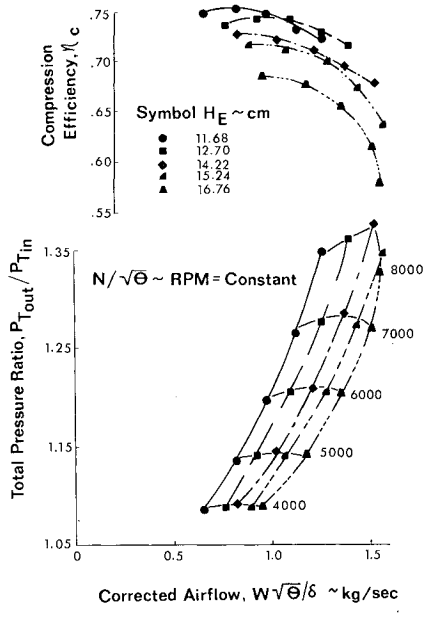

Fig. 4 Fan map for fan 4: $\theta_I = 105$ deg, $\theta_{LPC} = 75$ deg, $\theta_{HPC} = 50$ deg.

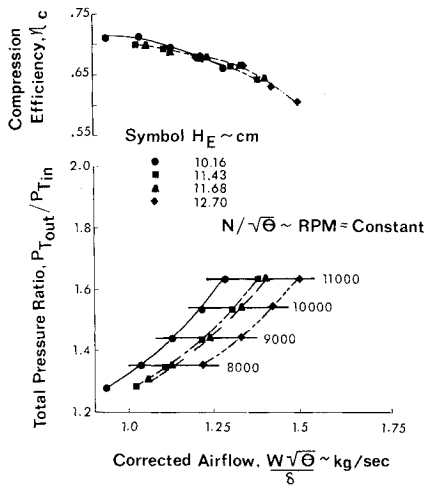

Fig. 5 Fan map for fan 6: $\theta_I = 105$ deg, $\theta_{LPC} = 75$ deg, $\theta_{HPC} = 50$ deg.

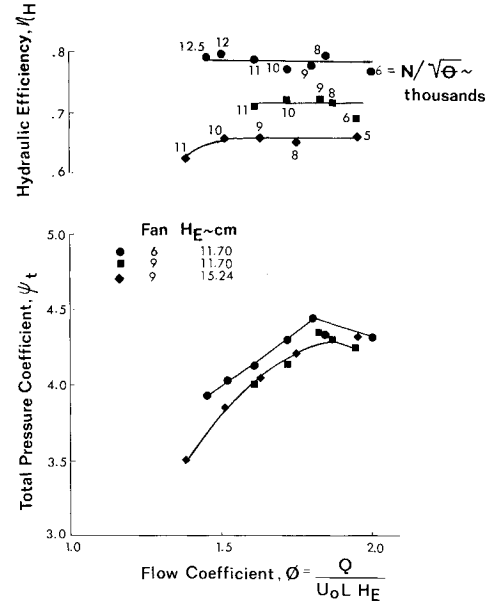

Fig. 6 Nondimensional performance based on exit height.

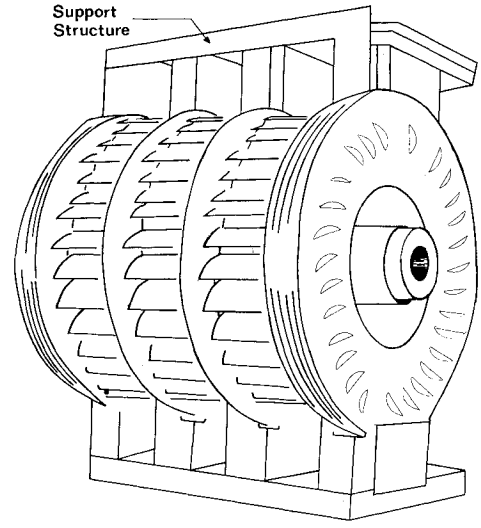

Fig. 7 Oblique view of 30.48 cm diameter, 30.48 cm span fan.

streamlines. In Fig. 9 the low-pressure recirculation is bounded in part by the streamline from point A to C and the high-pressure recirculation is bounded in part by the streamline from point B to D. The flow between those two streamlines is the "through flow" which is the useful output flow of the CFF. The flowfield surveys provided a detailed quantitative description of the flow in all of these regions.

A servo probe was used to measure total pressure, total temperature, and flow direction at centerline locations in the fan inlet, interior, and exit regions. Static taps in both the rotating front plate and the stationary back plate provided the necessary static pressure field.

Mach number and velocity at each point were calculated from static and total pressure and total temperature measurements. Streamlines were calculated by integrating flowfield properties from the center radially outward.

Figure 10 illustrates the flow nonuniformity for fan 6 at 12,500 rpm with an 11.68 cm exit height. The Mach numbers increase to about 0.6-0.8 at the discharge end of the inlet rotor blades and reach a maximum of 1.17 at the rotor center. The flow decelerates to 0.6-0.7 Mach number at the exit rotor blades. A shock inside the exit rotor blades near point C is suspected. The streamlines for the interior flow are shown in Fig. 11.

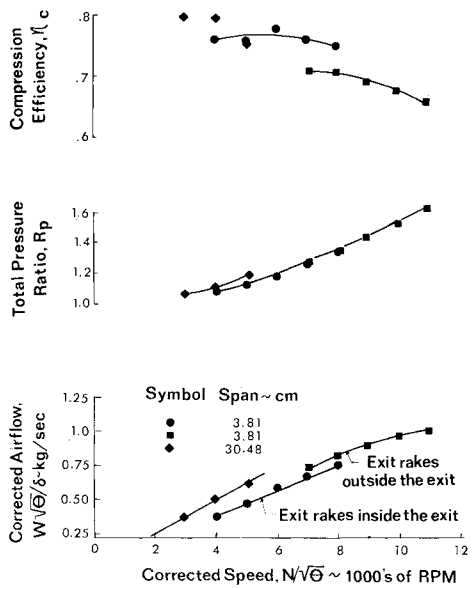

Fig. 8 Performance comparison summary of 30.48 and 3.81 cm span fans, $H_E = 10.16$ cm.

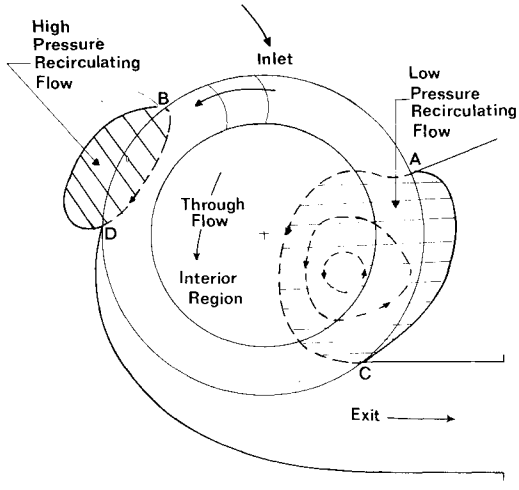

Fig. 9 Schematic of flow regions.

Flowfield Summary

The most obvious characteristics of the flowfield are:

1) Shockless transonic flow occurs in the interior region for fan 6 at 12,500 rpm with an exit height H_E of 11.68 cm, and for fan 9 at 11,000 rpm with $H_E = 15.24$ cm.

2) Maximum Mach number occurs near the rotor center.

3) Core static pressure gradients generally increase with increasing corrected airflow.

4) Static and total pressures are approximately equal in the vortex center and are well below ambient pressure.

Finite-Element Analytical Model

The experimental data presented in the previous sections illustrate the critical importance of the housing geometry on the performance of the CFF. Previous theoretical analyses of the CFF are summarized in detail in Ref. 4. In general, none of the previous analyses[6,10,12,13] correctly account for the influence of the fan housing or blade geometry on the flowfield. In view of the complex geometry of the housing, the analytical model was based on the finite-element method. The models developed in this study include a one-dimensional, compressible flow analysis and a two-dimensional, incompressible flow analysis.

One-Dimensional Finite-Element Analysis

The one-dimensional analysis was developed to analyze the effect of compressibility, area variation, wall shear stress, and the rotor blade force on the CFF performance.

The basic equations governing the flow are:

Continuity:

$$\dot{m} = \rho A u \tag{1}$$

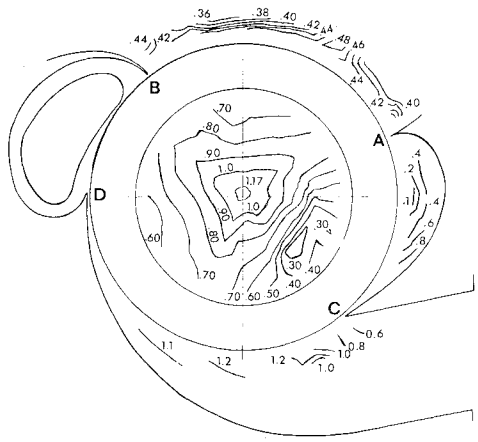

Fig. 10 Mach number field of fan 6, $H_E = 11.68$ cm, $N/\sqrt{\theta} = 12{,}500$ rpm.

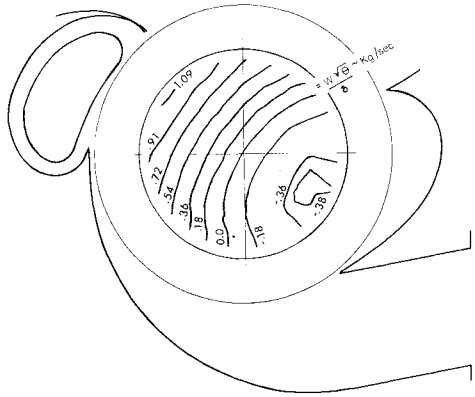

Fig. 11 Streamline field of fan 6, $H_E = 11.68$ cm, $N/\sqrt{\theta} = 12{,}500$ rpm.

Linear momentum:

$$\rho u\frac{du}{dx}=-\frac{dp}{dx}-C_f\frac{\rho u^2}{2}\frac{1}{A}\frac{dA_W}{dx}+\rho f \tag{2}$$

where $C_f=\tau_w/\frac{1}{2}\rho u^2$ is determined from the von Kármán-Nikuradse equation:

$$\frac{1}{\sqrt{4C_f}}=-0.8+2\log_{10}(Re_D\sqrt{4C_f}) \tag{3}$$

$$D_H=\frac{4A}{dA_w/dx} \tag{4}$$

Energy:

$$\rho u\left(\frac{dh}{dx}+u\frac{du}{dx}\right)=\rho u\left(\frac{dQ}{dx}\right)+\frac{\dot{q}_w}{A}\frac{dA_w}{dx}+\rho fu \tag{5}$$

where ρfu is the rate of work done by the rotor blade forces; fu is subsequently replaced by dw/dx. The thermodynamic state relations are:

$$\rho=\rho(p,T)$$
$$h=h(p,T) \tag{6}$$

The above equations can be combined to yield the following two differential equations for dp/dx and dT/dx (see Ref. 4 for details).

$$\frac{dp}{dx}\left[1-u^2\left(\frac{\partial\rho}{\partial p}\right)_T\right]+\frac{dT}{dx}\left[-u^2\left(\frac{\partial\rho}{\partial T}\right)_p\right]$$
$$=\frac{\rho u^2}{A}\frac{dA}{dx}-\frac{4\tau_w}{D_H}+\rho\frac{dw}{dx} \tag{7}$$

$$\frac{dp}{dx}\left[-u+\rho u\left(\frac{\partial h}{\partial p}\right)_T\right]+\frac{dT}{dx}[\rho uC_p]$$
$$=\rho u\left(\frac{dQ}{dx}\right)+\frac{4}{D_H}\dot{q}_w+\frac{4\tau_w u}{D_H} \tag{8}$$

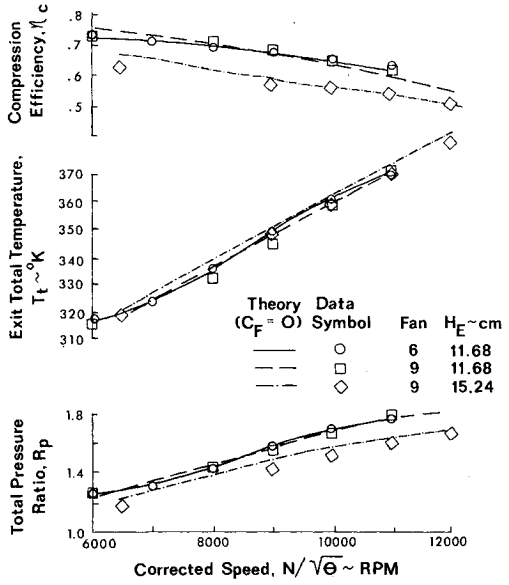

Fig. 12 Theory and data comparison of fans 6 and 9, $\theta_{LPC}=75$ deg, $\theta_{HPC}=50$ deg, $\theta_I=105$ deg.

The Galerkin or method of weighted residual technique is used in the following finite-element approach. The temperature and pressure variation across an element are approximated by linear polynomials, ϕ_i

$$p\approx\phi_i p_i=\{1-x/h,\ x/h\}\begin{Bmatrix}p_1\\p_2\end{Bmatrix}$$
$$T\approx\phi_i T_i=\{1-x/h,\ x/h\}\begin{Bmatrix}T_1\\T_2\end{Bmatrix} \tag{9}$$

where p_i and T_i are the discrete pressure and temperature values at node i.

Approximating $T(x)$ and p (x) by linear polynomials will result in an error in the differential equations. The inner product of the interpolation function and the differential equation is set equal to zero to minimize the approximation error. This procedure leads to the following equations for p_2 and T_2 (conditions at the downstream node) in terms of the values at the upstream node.

$$p_2=\left\{\left(\frac{\rho u^2}{A}\frac{dA}{dx}-\frac{4\tau_w}{D_H}+\rho\frac{dw}{dx}\right)\rho uC_p dx+\left(1-\frac{u^2}{RT}\right)p_1\rho uC_p\right.$$
$$\left.+\left(\rho u\frac{dw}{dx}+\frac{4\tau_w u}{D_H}\right)+\frac{4}{D_H}\dot{q}_w\left(\frac{-u^2\rho}{T}\right)dx+p_1u^3\left(\frac{\rho}{T}\right)\right\}$$
$$\Big/\left\{\left(1-\frac{u^2}{RT}\right)(\rho uC_p)+u^3\frac{\rho}{T}\right\} \tag{10}$$

$$T_2=\left\{\left[\rho u\frac{dw}{dx}\right]+\frac{4\tau_w u}{D_H}+\frac{4}{D_H}\dot{q}_w\right]dx\left(1-\frac{u^2}{RT}\right)+\rho uC_pT_1$$
$$\times\left(1-\frac{u^2}{RT}\right)+u\left(\frac{\rho u^2}{A}\frac{dA}{dx}-\frac{4\tau_w}{D_H}+\rho\frac{dw}{dx}\right)dx+u^3\rho\Big\}$$
$$\Big/\left\{\left(1-\frac{u^2}{RT}\right)(\rho uC_p)+\frac{u^3\rho}{T}\right\} \tag{11}$$

The above analysis was computerized. The bracketed coefficients were averaged across each element by an iterative procedure to keep errors to a minimum. Integrating through the rotors was accomplished by assuming the flow angles at the rotor tips (determined from test data or from the following two-dimensional analysis) and computing the work input as shown below:

For the inlet rotor:

$$\frac{dw}{dx}=\frac{U_2C_{z_2}\cos\alpha_2+U_1C_{z_1}\sin\alpha_1}{X_{R_2}-X_{R_1}} \tag{12}$$

For the outlet rotor:

$$\frac{dw}{dx}=\frac{U_1C_{z_2}\sin\alpha_4-U_2C_{z_1}\sin\alpha_3}{X_{R_4}-X_{R_3}} \tag{13}$$

These relations were determined from the power input.

$$\text{power}=\Omega\cdot\text{torque}=\dot{m}\Omega\left(C_{\theta_{\text{out}}}R_{\text{out}}-C_{\theta_{\text{in}}}R_{\text{in}}\right) \tag{14}$$

$$\frac{\text{power}}{\dot{m}}=C_{\theta_{\text{out}}}U_{t_{\text{out}}}-C_{\theta_{\text{in}}}U_{t_{\text{in}}} \tag{15}$$

Because the downstream flow properties are strongly dependent on area change and rotor blade force and the rotor blade force in turn depends on the downstream flow properties, a stable iterative procedure was developed to calculate the downstream flow properties.

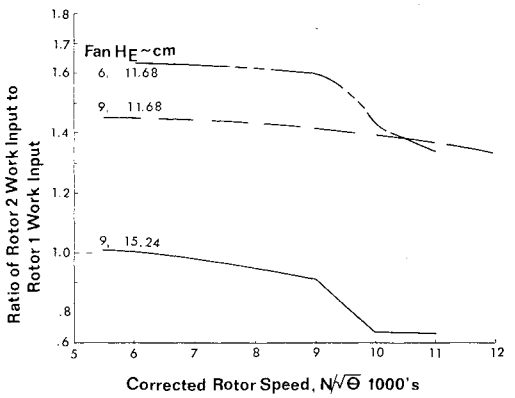

Fig. 13 Ratio of rotor 2 work input to rotor 1 work input vs rpm.

The area distribution for the CFF was determined from the experimentally determined streamlines inside the fan. A cubic spline curve fit was used to fit the area and area derivative distribution with X. Numerical experiments indicated that heat has to be added to the interior flow to increase the exit total temperature and to decrease the fan efficiency below one. Heating of the flow inside the interior is due to losses inside the rotating airfoils and convection from the hot recirculating flow in the cavity regions. This heat input was obtained from the experimental adiabatic efficiency measurements and is idealized by uniformly distributing it between the rotors.

The one-dimensional computer program was used to predict the overall performance for fans 6 and 9 with $H_E = 11.68$ cm and fan 9 with $H_E = 15.24$ cm. Good agreement with test data is obtained, as shown in Fig. 12. The inlet mass flow was determined from test data, and the experimentally measured flow angles on both sides of the inlet and outlet rotors were input. The ratio of the second rotor work input to that of the first rotor is plotted in Fig. 13 for the three configurations evaluated. Fan 6 has the highest ratio of about 1.6 for rpm below 9000. Fan 9 has a lower work ratio of about 1.4 and with a 15.24 cm exit has a much lower work ratio ranging 1.0-0.75. The lower ratio for the larger exit is associated with the decreased velocity through the second rotor due to an increased cross-sectional area associated with the 15.24 cm exit height. A large drop in work input ratio occurs for three of the four cases shown between 9000 and 10,000 rpm. This drop is associated with a general 6-9 deg decrease in α_2 (rotor 1 absolute outlet angle) and a 3-6 deg increase in α_3 (rotor 2 absolute inlet angle). These angles most likely change because of supersonic flow within the airfoils near point C.

Two-Dimensional Finite-Element Analysis

The major shortcoming of all but one of the previous analyses is that the effect of the housing on the flowfield has not yet been considered, the single exception being that of Ikegami and Murata.[12] Their analysis was limited to incompressible flow with linear housings which separated the inlet from the outlet. Extension of their analysis to an arbitrary housing shape is not practical.

In the present analysis the flow is considered to be steady and incompressible. The flow both outside and inside the fan is treated with a single formulation. The recirculation flows are not treated.

Consider flow through a row of stationary cascades. It is assumed that the flow is irrotational, i.e.

$$\nabla \times \underline{W} = 0 \qquad \text{where} \qquad \underline{W} = \underline{C} \tag{16}$$

For rotating airfoils, the velocity is transformed such that the rotors are stationary, i.e.

$$\underline{W} + \underline{U} = \underline{C} \qquad \text{or} \qquad \underline{W} = \underline{C} - \underline{U} \tag{17}$$

where $\underline{W}$ is the local relative velocity vector and $\underline{U}$ is the local tip velocity vector. The irrotational condition relative to the airfoils is

$$\nabla \times (\underline{C} - \underline{U}) = \nabla \times \underline{C} - \nabla \times \underline{U} = 0 \tag{18}$$

where

$$u = \psi_{,y} \qquad v = -\psi_{,x} \tag{19}$$

and

$$\nabla \times \underline{U} = 2\underline{W}_z \tag{20}$$

Thus using indical notation

$$\psi_{,ii} = 2\underline{W}_z \qquad i = 1, 2 \tag{21}$$

Integrating over the two-dimensional area Ω and using a weighting factor ϕ_N for each node N

$$\int_\Omega \psi_{,ii}\phi_N d\Omega - \int_\Omega 2W_z\phi_N d\Omega = 0 \tag{22}$$

Integrating the first term by parts to lower the order of differentiation and to introduce the stream function boundary conditions,

$$\int_\Omega \psi_{,ii}\phi_N d\Omega = \int_\Gamma \psi_{,i} n_i \overset{*}{\phi}_N d\Gamma - \int_\Omega \psi_{,i}\phi_{N,i} d\Omega \tag{23}$$

where the $\overset{*}{\phi}_N$ is the interpolation function on a boundary. Therefore,

$$\int_\Omega \psi_{,i}\phi_{N,i} d\Omega = \int_\Omega 2W_z\phi_N d\Omega + \int_\Gamma \psi_{,i} n_i \overset{*}{\phi}_N d\Gamma \tag{24}$$

The stream function ψ is now approximated by linear polynomials over a series of triangular elements

$$\psi \simeq \phi_i \psi_i \text{ with } \phi_i = a_i + b_i x + c_i y \tag{25}$$

which leads to the following set of matrix equations

$$\left\{\int_\Omega \phi_{N,i}\phi_{M,i} d\Omega\right\}\psi_M = [h(r-R_I) - h(r-R_o)] \int_\Omega 2W_z\phi_N d\Omega + \int_\Gamma \psi_{,i} n_i \overset{*}{\phi}_N d\Gamma \tag{26}$$

or

$$A^e_{NM}\psi_M = [h(r-R_I) - h(r-R_o)]\, a_N 2W_z \Omega^e + F^e_N \tag{27}$$

where $h(r-R_I)$ is the heaviside unit step function and R_o and R_i are the outer and inner rotor radii, respectively.

The line integral cancels everywhere but at the boundary. The boundary conditions used were the Dirichlet boundary conditions. The separating streamline positions, which segregate the through flow from the recirculating vortex flow, was determined from the test data.

The rotational matrix F^e_N is treated as a forcing function, i.e.

$$\begin{Bmatrix} F'_1 \\ F'_2 \\ F'_3 \end{Bmatrix} = 2A^{(e)} W_z \begin{Bmatrix} a_1 \\ a_2 \\ a_3 \end{Bmatrix} \tag{28}$$

where the flux vector

$$F_N = \int_\Gamma \psi_{,i} n_i \dot{\phi}_N d\Gamma \tag{29}$$

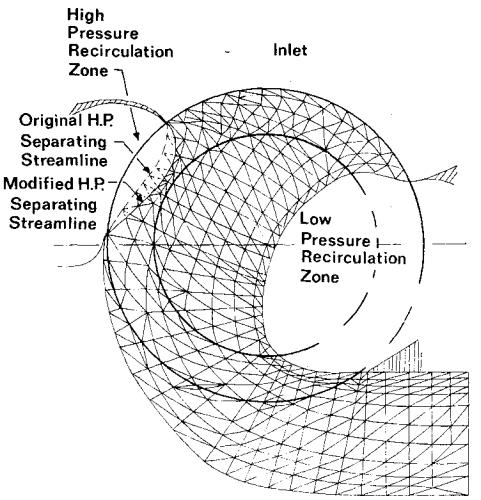

Fig. 14 Discretization of interior for finite-element analysis.

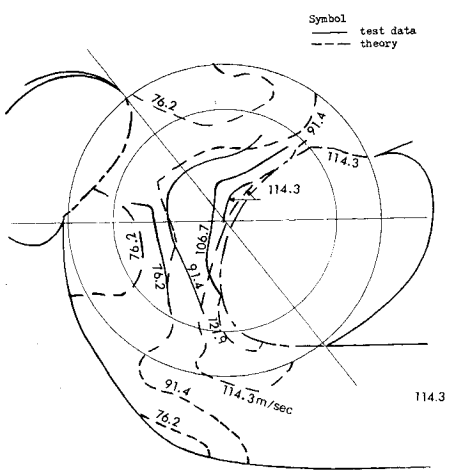

Fig. 15 Comparison of theory and test velocity data for fan 4, $H_E = 11.68$ cm, 4000 rpm.

is equal to the flow parallel to the boundary surface. For velocity perpendicular to the surface the line integral is equal to zero.

The above element equations were combined in a computer program. The results are presented below.

Analytical Results

The inlet and interior regions of the CFF were represented by triangular elements. The interior region discretization is illustrated in Fig. 14. The two regions were first considered together. The boundary conditions specified were a linear variation of ψ at the bellmouth inlet and exhaust duct exit, and the shapes of the low- and high-pressure separating streamlines were specified on the basis of test data and experience. The computed interior velocity contours were compared to the test data and it was determined that clockwise rotation of the interior streamlines was needed. Furthermore, because the influence of the rotor blades was not input as a boundary condition, the inlet and interior regions were next treated separately.

The functional shape of ψ vs θ at the rotor inlet was guided by test data and an understanding of the flow. A few computer runs were required to obtain close agreement with test data. The final ψ vs θ profile boundary condition at the rotor inlet was approximately parabolic. The high-pressure separating streamline position inside the rotor was also changed to lower the interior flow angles near the high-pressure cavity and to increase the velocity in its vicinity to effect a better data match. Good agreement between

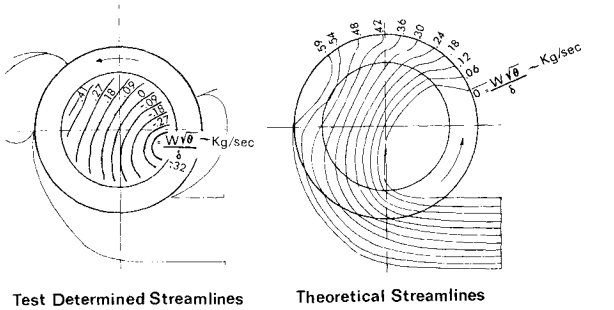

Fig. 16 Comparison of test and theoretical streamlines for fan 4, 4000 rpm.

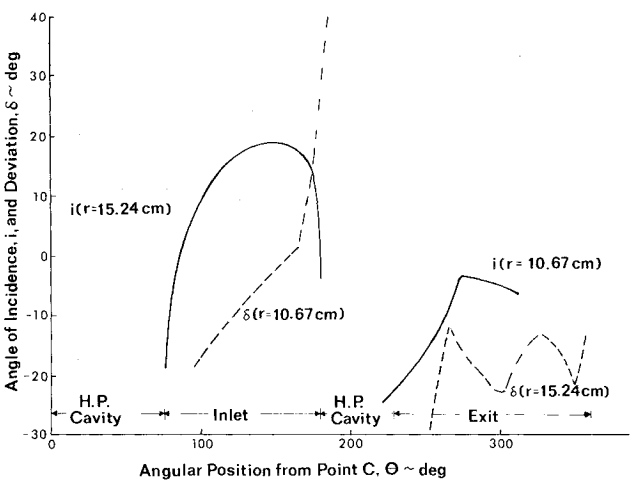

Fig. 17 Theoretical angles of incidence and deviation at rotor tips, fan 4, $H_E = 11.68$ cm, 4000 rpm.

theoretical and experimental velocity contours is shown in Fig. 15. The computed streamlines for the interior are shown in Fig. 16 to be in good agreement with test-determined streamlines.

The stream function boundary condition at the rotor inlet that best fit the data was found to be approximately represented by a quadratic. The inlet radial velocity profile can therefore be approximated by a linear variation with θ. A physical explanation for this boundary condition follows. The vortex sets up a velocity near the fan center of approximately twice the tip velocity (as observed experimentally). The rotor tip sets the flow velocity at the rotor tip (along a line of flow symmetry) equal to the rotor tip velocity. Therefore, a linear velocity variation across the interior flowfield is typical. A similar variation in the radial velocity in the inlet is therefore reasonable.

Angles of incidence and deviation were determined from the model just outside the airfoils. The flow velocities outside the rotors are used as large changes in circumferential velocity occur inside the airfoils. As shown in Fig. 17, the incidence angles vary from -20 to $+18$ deg in the inlet and from -25 to -5 deg in the exit. Deviation angles range from -30 to $+40$ deg. These large variations probably result in large internal flow losses which in turn lead to low compression efficiencies.

Conclusions and Recommendations

The experimental development studies reported herein extend the CFF performance into the transonic flow regime. Both measured performance changes with rpm, and the theoretical analysis indicates that choking occurs in the airfoils at the entrance of the exit duct. Housing modifications, interior guide vanes, airfoil geometry changes, and a variable geometry exit duct should be developed to increase performance in this flow regime.

The 30.48 cm span fan test results indicate that the performance results for the 3.81 cm span fan are pessimistic due to end wall effects.

Detailed flowfield measurements presented demonstrate the complicated two-dimensional nature of the flow. The flow properties in the low-pressure vortex indicate that large thermal energy conversion occurs due to viscous dissipation. The flowfield was similar at different rotational speeds until the above-mentioned flow separation occurred.

A compressible one-dimensional finite-element analysis was developed which predicted overall performance in good agreement with the test data. The analysis determines the work input at each rotor from a knowledge of the flow angles at the rotor tips. A relative decrease in the second-stage rotor work input was calculated for the 15.24 cm exit configuration due to the decrease in velocity through the rotor, as compared with the 11.68 cm exit data. The analysis indicated that large heating of the interior flow occurs. This heating is attributed to viscous dissipation in the rotating airfoils. More efficient airfoil design and interior guide vanes should increase performance considerably.

The two-dimensional finite-element analysis developed treats arbitrary housing and the fan rotor as an integrated unit. Good agreement between the predicted and test-determined flow properties was demonstrated. The boundary condition at the inlet rotor tips which best fit the test data was a linear radial velocity variation with angular position. The analysis should be extended to treat compressible flows with viscous dissipation and shock waves present. The improved analysis should consider the entire flow region.

Acknowledgments

The experimental investigation was conducted while the first author was employed by Vought Systems Division of LTV under NASC Contract N00019-74-C-0434. The authors wish to acknowledge the contributions of F. Isley, formerly with LTV, and K. Marsh of LTV, who were responsible for the test program. A portion of the computer costs was supported by Gulf Research.

References

[1] Dornier, P., "Multiple Drive for Aircraft Having Wings Provided with Transverse Flow Blowers," Patent 3,065,928 (USA), Nov. 27, 1962.

[2] Mortier, P., Patent DRP 146464 (France), 1892.

[3] Mortier, P., "Fan or Blowing Apparatus," Patent 507,445 (USA), Oct. 24, 1893.

[4] Harloff, G.J., "Cross Flow Fan Experimental Development and Finite Element Modeling," Ph.D. Dissertation, The University of Texas at Arlington, April 1979. Available from University Microfilms International, Ann Arbor, Michigan.

[5] Porter, A.M. and Markland, E., "A Study of the CFF," *Journal of Mechanical Engineering Science,* Vol. 12, No. 6, 1970, pp. 421-431.

[6] Coester, R., "Theoretical and Experimental Studies of Cross-Flow Blowers," *Mittelungen aus dem Institut fur Aerodynamik,* Federal Polytechnic Institute, Zurich, 1959, No. 28, (in German).

[7] Laasko, H., "Querstromventilatoren mit Druckkenwerthe 4," Heizung, Luftung, Haustechnik, 1957, Seite 324/325.

[8] Eck, B., *Fans,* Pergamon Press, Elmsford, N.Y., 1973.

[9] Ackert, J., "Present and Future Problems of Aircraft Propulsion," *Schweizerische Bauzeitung,* Heft 1, Band 112, 1938.

[10] Ilberg H. and Sadeh W.Z., "Flow Theory and Performance of Tangential Fans," *Proceedings of the Institute of Mechanical Engineers,* Vol. 180, Part 1, No. 19, 1965-1966.

[11] Englehardt, W., "Experimental Test in Cross Flow Blowers with Varying Reynolds Numbers," Ph.D. Dissertation, University of Karlsruhe, Federal Republic of Germany, July 1967 (in German).

[12] Ikegami, H. and Murata, S., "A Study of Cross Flow Fans," *Technology Reports of the Osaka University,* Japan, Faculty of Engineering Technology Reports, Vol. 16, Oct. 1966, pp. 551-578.

[13] Harloff, G.J. and Wolfe, G.W., "Study to Develop a CFF Analysis Method," Vought Corp., Systems Div., Report 2-57110/6R-3297, April 1976.